OSIRIS observations of OH $A^2\Sigma^+$–$X^2\Pi$ 308 nm solar resonance fluorescence at sunrise in the upper mesosphere[1]

R.L. Gattinger, C.D. Boone, K.A. Walker, D.A. Degenstein, N.D. Lloyd, P.F. Bernath, and E.J. Llewellyn

Abstract: Since the OH molecule plays a critical role as a catalyst in atmospheric photochemistry, an accurate measurement of the OH density profile covering a broad range of latitudes and solar local times is required to quantify the major reactions involved. The optical spectrograph and infra-red imager system (OSIRIS) instrument on the Odin satellite observes scattered solar radiation at the terrestrial limb from the upper troposphere, the stratosphere, and the mesosphere. The wavelength range, 275 nm to 810 nm includes the OH $A^2\Sigma^+$–$X^2\Pi$ 0–0 band at 308 nm, which is seen in solar resonance emission superimposed upon the underlying atmospheric Rayleigh-scattering background. OSIRIS routinely detects the OH 308 nm emission in the mesosphere from sunrise through to sunset. One feature of the OH diurnal variation is a nocturnal layer in the 80–85 km region that is frequently, but not always, detectable in solar resonance for a short period following sunrise — the feature we label here as the "sunrise flash". This paper describes the observational analysis procedures involved in the quantitative measurement of the OSIRIS OH profiles together with a broad overview of the variability of the feature at sunrise. Also included is a photochemical model simulation of the OH sunrise layer using background atmospheric parameters, especially the water vapour mixing ratio, provided by the ACE/FTS instrument on the Canadian SCISAT satellite. For a number of nearly coincident measurements between OSIRIS OH and ACE/FTS water vapour, the model simulations show general agreement between the two. Agreement is improved by modifying the eddy mixing rates in the 80–85 km region, commensurate with the expected range of mixing rates.

PACS Nos.: 42.68.Ay, 82.20.Pm, 82.30.Cf, 82.33.Tb, 92.60.H−, 92.60.Ta

Résumé : Puisque la molécule OH joue un rôle critique comme cataliseur dans la photochimie atmosphérique, nous avons besoin de mesurer de façon précise le profil de densité de OH sur une large bande de latitude et de temps solaire afin de quantifier les réactions importantes

Received 30 November 2005. Accepted 15 October 2006. Published on the NRC Research Press Web site at http://cjp.nrc.ca/ on 5 April 2007.

R.L. Gattinger, D.A. Degenstein, N.D. Lloyd, and E.J. Llewellyn.[2] ISAS, Department of Physics and Engineering Physics, University of Saskatchewan, Saskatoon, SK S7N 5E2, Canada.
C.D. Boone, K.A. Walker, and P.F. Bernath. Department of Chemistry, University of Waterloo, Waterloo, ON N2L 3G1, Canada.

[1]This paper is published as part of the proceedings of the 32nd Annual European Meeting on Atmospheric Studies by Optical Methods (ASOM) that was held 29 August to 1 September 2005 at the University of Western Ontario, London, Ont.

[2]Corresponding author (e-mail: edward.llewellyn@usask.ca).

 doi: 10.1139/P06-087

pertinentes. L'instrument OSIRIS sur le satellite Odin observe la radiation solaire diffusée au limbe terrestre de la haute stratosphère, de la stratosphère et de la mésosphère. Le domaine de longueur d'onde, 275 nm à 810 nm, inclut la bande $A^2\Sigma^+$–$X^2\Pi$ 0–0 à 308 nm, qui est détectée dans l'émission de résonance solaire surimposée sur le fond de diffusion Rayleigh de l'atmosphère. OSIRIS détecte de façon routinière l'émission à 308 nm du OH dans la mésosphère du lever au coucher du soleil. Une caractéristique de la variation diurne est une couche nocturne dans la région 80-85 km qui est fréquemment, mais pas toujours, détectable dans la résonance solaire pendant une courte période suivant le lever du soleil — caractéristique baptisée « éclair de l'aube ». Nous présentons ici les procédures d'analyse impliquées dans les mesures quantitatives des profils de OH par OSIRIS, incluant une large revue des variations au lever du soleil. Nous incluons aussi une simulation du model photochimique de la couche de OH au lever du soleil en utilisant des paramètres de fond atmosphérique, spécialement le rapport de mélange de vapeur d'eau fourni par l'instrument ACE/FTS à bord du satellite canadien SCISAT. Pour un bon nombre de mesures coïncidentes de la vapeur d'eau entre OSIRIS et SCISAT, la simulation indique un excellent accord entre les deux. Cet accord s'améliore par la modification des taux de mélange par tourbillon dans la région entre 80 et 85 km, compatible avec le domaine de taux de mélange.

[Traduit par la Rédaction]

Introduction

Early observations of the OH 0–0 band solar-resonance fluorescence at 308 nm were obtained by Anderson [1] with a rocket-borne zenith viewing spectrometer. Morgan et al. [2] reported resonance fluorescence observations of mesospheric OH using the imaging spectrometric observatory (ISO) on the ATLAS 1 mission. A more extensive study was conducted with the middle-atmosphere high-resolution spectrograph investigation (MAHRSI) instrument by Conway et al. [3, 4] on two space shuttle flights in 1994 and 1997. Rotational lines of the band were spectrally resolved and with the aid of a high-resolution solar spectrum [5] it was possible to make a detailed comparison between observed line intensities and the calculated rotational emission rate g-factors. Nearly global height profiles of OH in the upper stratosphere and mesosphere were obtained by the MAHRSI instrument. Summers et al. [6] used the MAHRSI results to examine the photochemistry in relation to previous analyses and proposed modifications to the accepted reaction rates to address both the model OH excess and the model ozone deficit.

Jucks et al. [7] observed the dominant odd hydrogen species from a balloon platform in the upper stratosphere and proposed a reaction rate set to explain their observations. Cageao et al. [8] and Li et al. [9] observed the OH column abundances using a ground-based Fourier transform spectrometer, so potentially providing a long term data base of OH variability. Brinksma et al. [10] and Hoppe et al. [11] detected a nocturnal OH layer in the 80 km region just after sunset using 308 nm light detection and ranging (LIDAR) systems. The microwave limb sounder (MLS)/Aura instrument observes OH with the THz module [12, 13] while HO_2 is observed with the 640 GHz radiometer. The Aura satellite mission [14] will thus provide major advances in our understanding of the atmospheric chemistry of the HO_x odd hydrogen species ($HO_x = OH + HO_2 + H$), especially in the upper stratosphere and lower mesosphere. Gattinger et al. [15] identified the OH 308 nm band in the OSIRIS spectra and have shown that these data can be used to study diurnal, seasonal, and geographic OH variations, especially in the upper mesosphere. In spite of these numerous studies, the actual production and loss rates of HO_x remain uncertain.

The optical spectrograph and infra-red imager system (OSIRIS) [16], a moderate resolution spectrograph compared to the MAHRSI instrument, does not resolve the rotational lines of the 308 nm band and, therefore, relies on the validated MAHRSI g-factors in the analysis. Also, the moderate resolution limits the useful OSIRIS OH observations to the region above approximately 55 km due to the dominant Rayleigh-scattering background at lower altitudes.

Fig. 1. A window of OSIRIS calibrated spectra from 74, 82, and 90 km limb tangent altitudes covering the wavelength range of the OH $A^2\Sigma^+$–$X^2\Pi$ 0–0 band at 308 nm. The observations are from 21 April 2005, 00:04 UT, 06:18 LT, 90.4° SZA, 22.1° south latitude, 93.3° east longitude. The Rayleigh reference spectra are scaled for each altitude at 306 and 312 nm. The excess signature in the 82 km spectrum at 308 nm is identified as the OH 0–0 band. Limb radiances at 90 km still retain adequate signal-to-noise to clearly identify the Rayleigh-scattered solar spectrum.

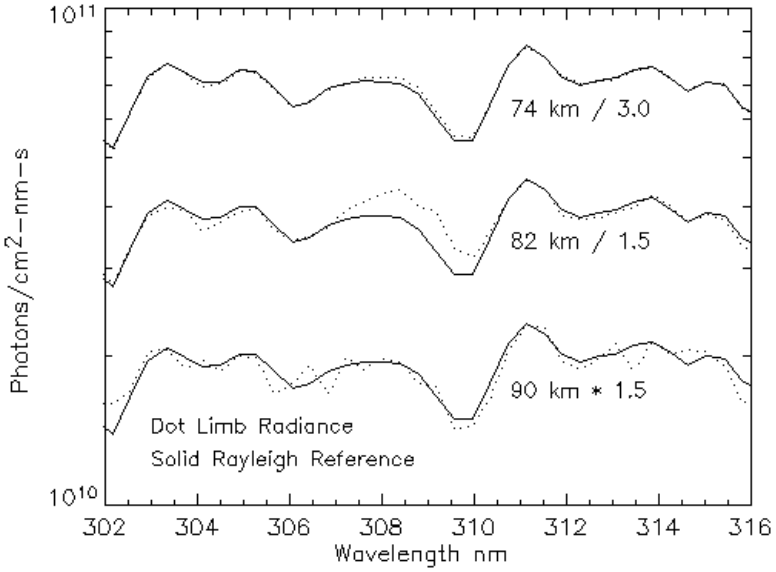

OSIRIS on the Odin satellite [17] is now a multiyear mission, the data set contains new information on the global distribution of mesospheric OH including the diurnal variations. This present study is limited to the newly identified OH 308 nm feature in the 80–85 km region immediately following sunrise, a flash-like event that disappears within 1 h after sunrise. The observational analysis techniques employed to derive OH vertical profiles from the OSIRIS limb observations are presented here, followed by a broad overview of the OH sunrise flash.

The OSIRIS OH profiles are also compared with model simulations of the OH layer using background atmospheric parameters derived from measurements by the atmospheric chemistry experiment/Fourier transform spectrometer (ACE/FTS) instrument [18] on the Canadian SCISAT satellite. The satisfactory comparison and (or) agreement between observations and model predictions provides another example of the substantiation of the accuracy of photochemical models developed over the past few decades (see, for example, refs. 19 and 20).

OH density profiles from OSIRIS limb radiance observations

The Odin satellite is in a 600 km sun-synchronous dusk/dawn orbit with ascending node at approximately 18:00 local time (LT), descending node at 06:00 LT and orbital inclination of 97.8°. OSIRIS on Odin measures limb-scattered solar radiation from the upper troposphere, the stratosphere, and the mesosphere over the wavelength range 275 nm to 810 nm with approximately 1 nm spectral resolution and a vertical field of view corresponding to 1 km at the tangent point. With a vertical limb scan rate of approximately 0.75 km/s and a nominal 2 s exposure time at mesospheric altitudes, a vertical resolution of approximately 3 km is achieved in the mesosphere. The limb altitude accuracy is typically better than 0.5 km. Routine observations of the mesospheric region, which began near the end of 2001, are conducted for a 24 h period at approximately 8 day intervals.

The adopted analysis procedures are similar to those described by Gattinger et al. [15]. Summarizing

Fig. 2. The spectra shown in Fig. 1 are repeated here but with the Rayleigh background removed. The OH $A^2\Sigma^+$–$X^2\Pi$ 0–0 band at 308 nm is clearly detected in the 74 and 82 km spectra but is absent in the 90 km spectrum. The baseline noise in the 74 km spectrum results from the detected electron statistics in the large underlying Rayleigh background signal, which is approximately 50 times larger than the OH resonance scatter signal (see Fig. 1).

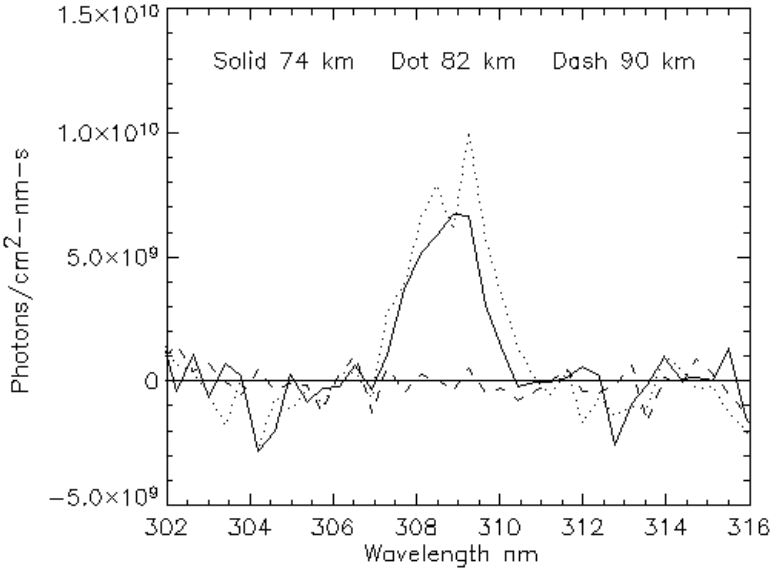

briefly, OSIRIS preflight absolute spectral calibrations are updated by comparison against a 55 km tangent limb radiance model using the European centre for medium-range weather forecast (ECMWF) data base [21]. Rayleigh background reference spectra from 45 km tangent altitude are used to isolate the OH 308 nm emission from the combined solar Rayleigh-scattered light and OH solar resonance emission. The estimated uncertainty in the derived OH densities is 11% in the upper mesosphere.

A series of spectra obtained by OSIRIS during a single limb scan covering a period of approximately 2 min on 21 April 2005, 00:04 UT, 06:17 LT, 90.6° solar zenith angle (SZA), 22.8° south latitude, 93.1° east longitude, interpolated to a 1 km tangent altitude grid, are shown in Fig. 1. Spectra at three altitudes, 74, 82, and 90 km are shown together with the normalized Rayleigh spectrum for each altitude. The spectrum at 82 km clearly indicates an enhancement in the 308 nm region. This excess signal is identified as the signature of the OH $A^2\Sigma^+$–$X^2\Pi$ 0–0 band sunrise flash. The excellent overlap of the solar features outside the OH band region is an indication of the high signal-to-noise ratio inherent in the OSIRIS data. At 90 km the noise in the spectrum is clearly present and indicates that the detection limit is being approached.

The limb radiance spectra obtained after removal of the Rayleigh background from the limb signals presented in Fig. 1 are shown in Fig. 2 for the same tangent altitudes. The OH 308 nm 0–0 band is clearly evident. The noise in the difference spectra arises from the combined effects of small errors in the background spectrum and the known detected electron noise statistics. These noise properties are included in the next step, the inversion procedure.

Inverting the OH limb radiance data to obtain vertical OH density profiles is accomplished with the aid of a forward model of the OH $A^2\Sigma^+$–$X^2\Pi$ 0–0 band limb radiance profiles, with background atmospheric parameters obtained by the ACE/FTS instrument. The model limb radiance is compared iteratively with the observed OH limb radiances to derive the OH density profiles. The Stevens and Conway [5] MAHRSI rotational emission rate g-factors are assumed. The OSIRIS OH density profile obtained from the sequential limb spectra for a single limb scan, a subset is shown in Figs. 1 and 2, is

Fig. 3. The OH limb radiance vertical profile compiled from the 308 nm 0–0 band intensities at all altitudes (subset shown in Fig. 2) is inverted here to produce the OH vertical density profile. The error bars include detected signal electron statistics and the estimated 11% overall uncertainty.

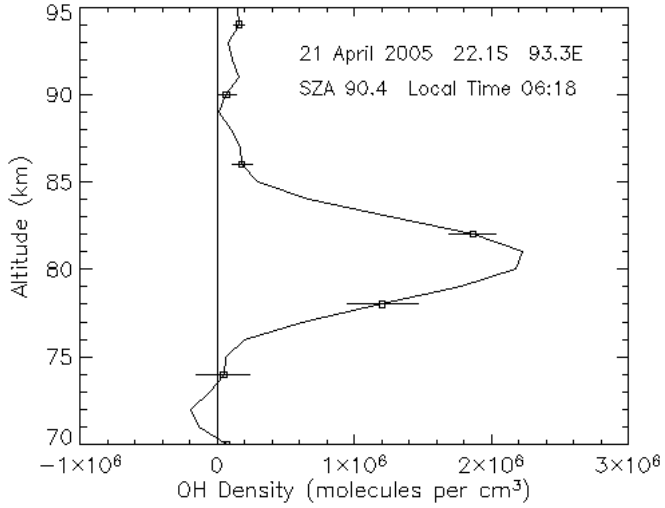

shown in Fig. 3. The error bars include the electron noise and the estimated 11% uncertainty discussed by Gattinger et al. [15].

OH sunrise density profiles

For the Odin orbit, sunrise occurs in the equatorial region with the time duration since sunrise varying slowly with latitude at low to mid-latitudes. To study the OH variability as a function of time after sunrise it is thus necessary to include a broad range of latitudes. A series of OSIRIS OH observations from 24–25 August 2005 have been chosen to cover from 30° south latitude to 50° north latitude where the duration from observation location to sunrise varies by approximately 50 min, a period sufficiently long to demonstrate the OH sunrise flash.

The observed OH profiles, ordered by time since sunrise, are shown in Figs. 4*a*–4*d*. Error bars, omitted here to improve the appearance of the figures, are similar to those in Fig. 3. Approximate time bins in minutes after sunrise for the four figures, respectively, are from 0 to 12 min, from 12 to 24 min, from 24 to 36 min, and from 36 to 48 min. While many profiles show very little, if any, enhancement in the 80–85 km region in any of the four time bins, those profiles that do show enhancements tend to occur in the earlier time bins. In Fig. 4*d*, the latest after sunrise, there does not appear to be any clear enhancement in the 80–85 km region. We apply the label "sunrise flash" to this intermittent OH sunrise transient in the upper mesosphere.

The OH density in the 65 km region increases gradually with increasing time after sunrise as the sunlight penetrates deeper into the atmosphere. The photochemical model discussed below predicts this behaviour, although the present study is limited to the 80–85 km region.

Comparisons of observations with photochemical model

A mesospheric one-dimensional time-dependent photochemical model is used to examine the dominant processes controlling the HO_x, O, and O_3 diurnal variations in the upper mesosphere [15]. Reaction rates for the model are mainly obtained from Sander et al. [22]. For this study, the rates are retained as published, that is, no rate modifications are made. Lyman α flux data are taken from the solar radiation and climate experiment (SORCE) data base [23]. Solar photodissociation rates are recalculated

Fig. 4. The observed OH density profiles are shown, these are ordered by time after sunrise into four 12 min bins from 0 to 48 min: Figure 4*a* from 0 min to 12 min, 4*b* from 12 min to 24 min, 4*c* from 24 min to 36 min, and 4*d* from 36 min to 48 min after sunrise. The noise limit of the observations as seen in the 90–95 km region is approximately 2×10^5 OH molecules per cm^3. In the earliest time bin most of the profiles show excess signal in the 80–85 km region while in the latest time bin there is little if any indication of this excess signature. The variability of the profiles is typical of the OH sunrise solar resonance signal.

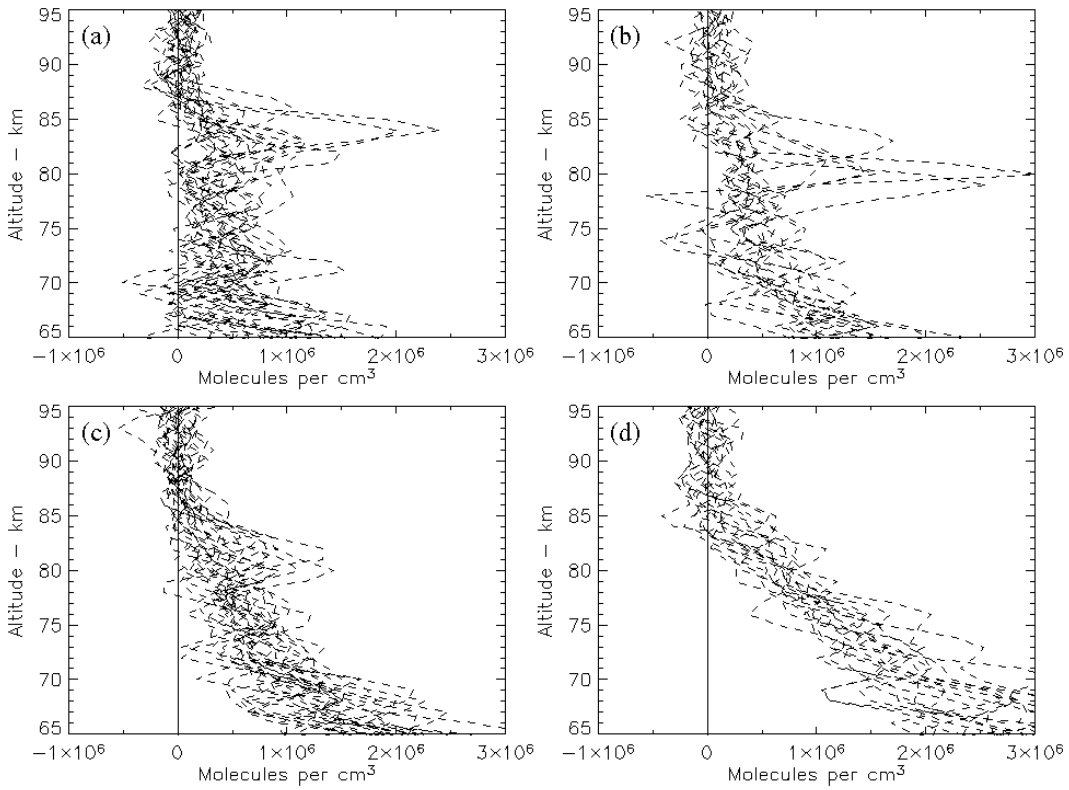

for each 1° change in SZA. Neutral density and temperature are from the ACE/FTS measurements. Diurnal repeatability in the model results is typically achieved by the third simulation day. However, above 85 km H and O lifetimes are sufficiently long that several additional simulation days are required for repeatability. The model vertical grid of 2 km is smoothed to approximately 3 km to simulate the OSIRIS vertical resolution.

For the eddy-mixing coefficient simulations, a simplified linear-log vertical profile is assumed that increases from 3.2×10^4 cm^2/s at 50 km to 1.0×10^6 cm^2/s at 100 km [24]. This profile is defined here as the default mixing-rate profile. The default profile is scaled by 1, 1/3, and 1/10 in the model comparisons to investigate the impact of variable eddy-mixing. Medvedev and Greatbatch [25] show that large variations in eddy-mixing can be expected in the upper mesosphere, especially in the equatorial region. Vertical motions caused by atmospheric tides, in the range of 1 km or less at 80 km altitude [26, 27] are not considered here.

Since the OH profile in the 80 km region is driven by the water vapour mixing ratio it is essential to know the latitudinal distribution of the water vapour mixing ratio to avoid confusion between temporal and spatial effects. The upper mesospheric water vapour mixing ratio used in the model calculations is measured by the ACE/FTS instrument. The ACE/FTS operates in occultation mode measuring solar infrared absorption spectra at the terrestrial limb in the 750–4400 cm^{-1} range, it thus obtains vertical

Table 1. OSIRIS and ACE/FTS observations, 20–21 April 2005 at 80 km.

	OSIRIS				ACE/FTS		
Profile	Latitude	Longitude	SZA	UT	Latitude	Longitude	UT
1	−22.1°	93.3	90.4°	00:04	−19.4°	94.0	23:59
2	−21.2°	165.8	90.1°	19:15	−21.1°	167.8	19:06
3	−16.3°	142.8	88.3°	20:50	−20.5°	143.2	20:44
4	−22.9°	44.9	90.7°	03:16	−18.3°	44.9	03:15
5	−11.1°	287.0	86.4°	11:16	−15.6°	282.0	11:24

Fig. 5. The measured ACE/FTS water vapour mixing ratio (parts per million by volume) for Profiles 1 through 5, as identified in Table 1, are used as inputs to the photochemical model. The error bars, shown on Profile 1 only, are similar for all five profiles. These profiles, which were obtained over a 16 h period, a 5.5° latitude range, and a 250° longitude range (Table 1), show considerable water-vapour variability in the 80 km region.

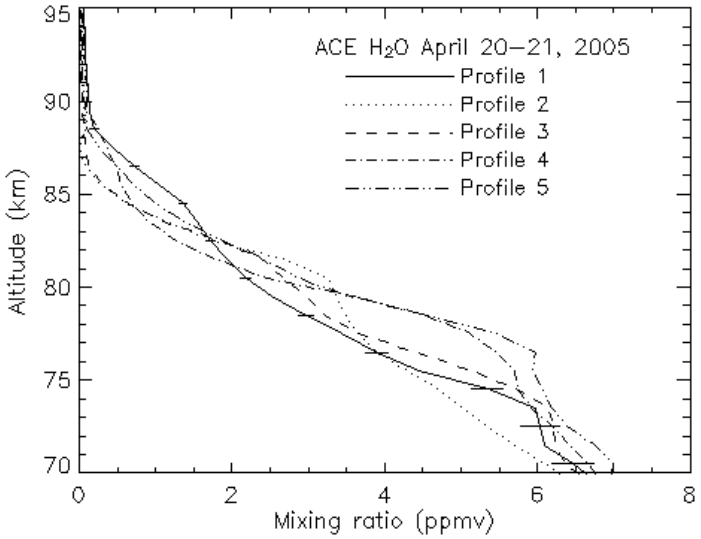

profiles of numerous species, including water vapour [28]. Vertical sampling ranges from 2 km to 6 km approximately matching the ACE/FTS vertical field of view of 4 km. Absolute limb-pointing knowledge for ACE/FTS is known to better than 0.5 km.

A detailed model versus observation comparison is done for five OSIRIS sunrise limb-scan profiles (Table 1) obtained on 20–21 April 2005. During this period, five ACE/FTS sunrise occultations (Table 1) are in good time and space coincidence with the OSIRIS observations. The ACE/FTS water-vapour-mixing ratio profiles for these five cases are shown in Fig. 5. These profiles exhibit considerable variability in the 80 km region.

A comparison between OSIRIS Profile 1 (from Fig. 3) and the model OH profiles, which assume the ACE/FTS Profile 1 for the water-vapour-mixing ratio, is shown in Fig. 6. The model profiles are calculated for three eddy mixing rates to demonstrate the effect of vertical mixing in the upper mesosphere. For eddy/10 the model profile is 3 km too high but by increasing the mixing rate to eddy*1 the layer altitude drops by 3 km. Thus, for the Profile 1 comparison pair the default eddy rate is the better choice.

The dependence of the model OH sunrise density on the water vapour mixing ratio is also included in Fig. 6. From Fig. 5 the ACE/FTS mixing ratio for Profile 2 at 80 km is considerably larger than

Fig. 6. OSIRIS Profile 1 is compared with model Profile 1 for an assumed eddy-mixing coefficient of 3×10^5 cm^2/s at 83 km, scaled by 1, 1/3, and 1/10. The model profiles are for 90.4° SZA to match the OSIRIS Profile 1 observation given in Table 1. The eddy-mixing rate scaled by unity gives the best match with OSIRIS Profile 1.

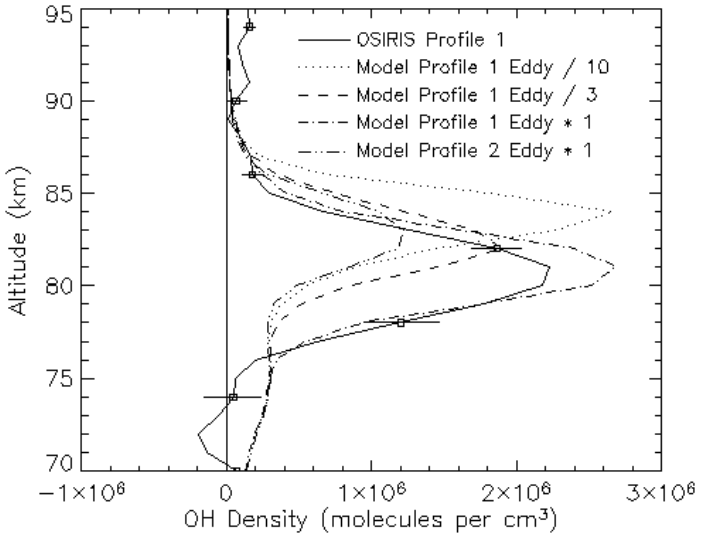

that for Profile 1. The change in the model OH profile, with eddy*1 for both cases, is very apparent in Fig. 6 and emphasizes the effect of the water-vapour-mixing ratio on OH sunrise density in the upper mesosphere.

A similar analysis, not shown here, was completed for OSIRIS Profiles 2 to 5 and matching ACE/FTS Profiles 2 to 5. For the Profile 2 pair the preferred mixing rate is nearer to eddy/3, which differs from the mixing rate required to match OSIRIS Profile 1 as discussed above. For the Profile 3 pair, the best match is obtained with the eddy/3 mixing rate. For Profile 4 the comparison is inconclusive as the observed OH density does not show a clear layer structure in the 80–85 km region. For Profile 5, the eddy*1 mixing rate gives a good altitude match but the magnitude is too large, above the OSIRIS Profile 5 error bar upper limit. It is interesting to note that the two profiles that require the higher eddy-mixing rates, Profiles 1 and 5, are also the two profiles in Fig. 5 with the largest water-vapour-mixing ratios at 85 km. These observed larger water-vapour-mixing ratios are the likely result if vertical eddy mixing is increased.

The diurnal variations at 80, 82, and 84 km for model Profile 1 are shown in Figs. 7–9, respectively, for eddy-mixing rates scaled by unity and by zero. At 80 km, the OH density increases rapidly for several hours after sunset but then decreases for the remainder of the night. This decrease is particularly rapid if the eddy-mixing rate is very low, with the resultant effect that at sunrise the OH density is depleted and the OH 308 nm solar resonance is very weak. At 82 km the OH density continues to increase throughout the night for unity eddy scaling and falls off slowly after sunrise producing a persistent OH 308 nm sunrise signal. For no eddy-mixing at 82 km, the OH density peak occurs before sunrise, this will result in a very weak OH 308 nm sunrise signal. At 84 km the OH density increases very slowly throughout the night and in this case the OH 308 nm sunrise signal is larger with no eddy-mixing.

The diurnal variations of OH, H, and O at 80 km altitude predicted by the model for ACE/FTS Profile 2 (high-water-mixing ratio at 80 km) and Profile 1 (low-water-mixing ratio at 80 km) are shown in Fig. 10. The model simulation, for both of the profiles, assumes eddy-mixing scaled by unity. Each case exhibits a sharp OH density peak shortly after sunset, the higher water-vapour-mixing ratio of

Fig. 7. The diurnal variation at 80 km for model Profile 1 shows the changes driven by two different eddy-mixing rates. The vertical bars indicate the times of geometric sunrise and sunset. The approximate pre-midnight OH LIDAR observations by Brinksma et al. [10] are included for comparison.

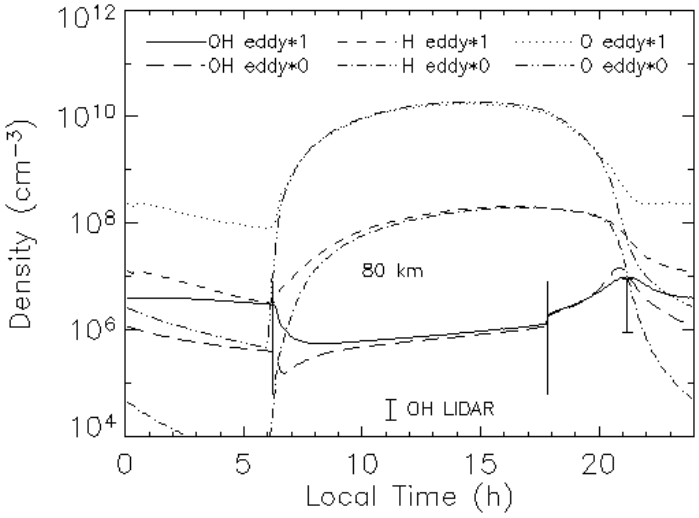

Fig. 8. The diurnal variation at 82 km for model Profile 1 again shows the changes driven by two different eddy mixing rates. The vertical bars indicate the times of geometric sunrise and sunset. The approximate pre-midnight OH LIDAR observations by Brinksma et al. [10] are included for comparison.

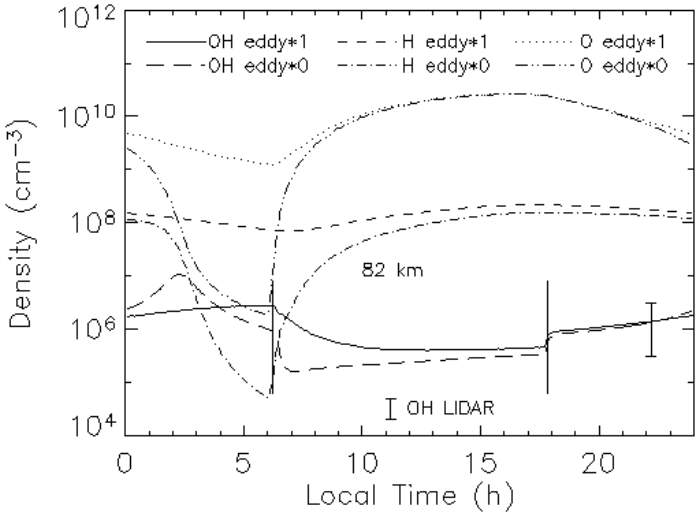

Profile 2 occurring within 1 h after sunset. The effect at sunrise is for the OH density to be very low with the larger water-mixing ratio. Thus, variations in the OH sunrise layer at 80 km are, at least in part, controlled by the water-vapour-mixing ratio.

The OH nocturnal variation near the density peak of the sunrise layer can be expressed in terms of the time constant for the removal of atomic oxygen through the O + OH reaction. If the catalytic removal rate of atomic oxygen is sufficiently fast to cause significant depletion of atomic oxygen before sunrise then the balance between OH and H is tipped in favour of OH and there is rapid loss of HO_x through OH + HO_2. The signature of the combined effects of this chain of events is a peak in the

Fig. 9. The diurnal variation at 84 km for model Profile 1 again shows the changes driven by the two different eddy mixing rates. The vertical bars indicate the times of geometric sunrise and sunset. The approximate pre-midnight OH LIDAR observations by Brinksma et al. [10] are included for comparison.

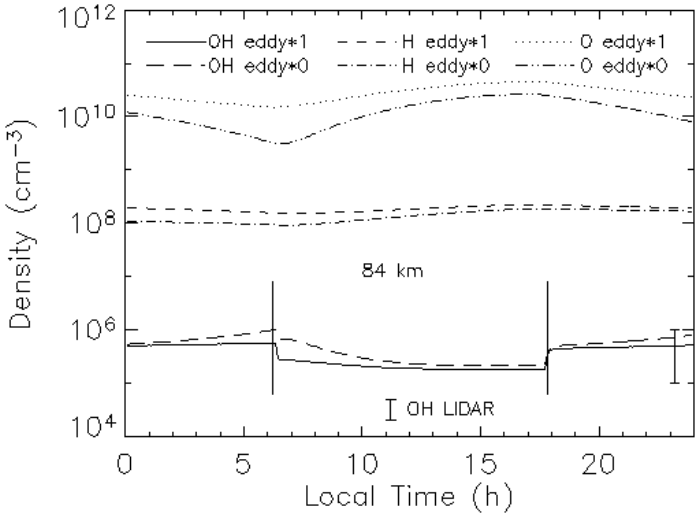

Fig. 10. The diurnal variations at 80 km for model Profile 1 (low-water-mixing ratio at 80 km) and Profile 2 (high-water-mixing ratio at 80 km) show the changes driven by the two different water-vapour profiles. Both cases assume eddy-mixing rates scaled by unity. The comparison shows that the time of occurrence of the nocturnal OH peak is influenced by the water-vapour-mixing ratio. The vertical bars indicate the times of geometric sunrise and sunset. The pre-midnight OH LIDAR observations by Brinksma et al. [10] are included for comparison.

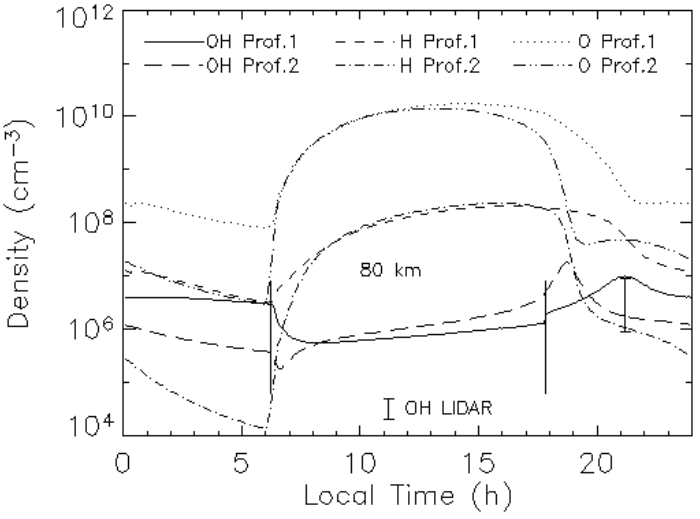

nocturnal OH density coincident with a major reduction in H and O. A check of this is provided by the time constant for atomic oxygen removal via O + OH, calculated as the inverse product of the O + OH reaction rate, and the OH density just after sunset. This time constant is found to be in good agreement with the time of the OH nocturnal peak relative to sunset, particularly for the smaller eddy mixing rates.

Conclusions

The upper mesospheric OH $A^2\Sigma^+$–$X^2\Pi$ 0–0 solar resonance fluorescence band at 308 nm is detected by the OSIRIS instrument just after sunrise. The layer width in the 80–85 km region is only a few kilometres and the layer density varies considerably with latitude and longitude. The resonance feature is very short-lived, it disappears in less than 1 h after sunrise. It is identified here as the "sunrise flash".

This OH sunrise layer is satisfactorily predicted by a one dimensional, time-dependent photochemical model that uses the ACE/FTS water-vapour profiles that are nearly coincident with the OSIRIS OH observations. The OH sunrise density is shown to depend on the water-vapour-mixing ratio. The fact that it is also necessary to adjust the vertical eddy-mixing rate to get improved agreement between model and observation for the various profiles, all over a very narrow latitude range but broad longitude range, suggests that the eddy-mixing rate is not zonally uniform. Neither is the water-vapour-mixing ratio zonally uniform in the 80 km region, this further suggests a variation in eddy-mixing rate.

Acknowledgements

This work was supported by the Canadian Space Agency and the Natural Sciences and Engineering Research Council (Canada). Odin is a Swedish-led satellite project funded jointly by Sweden (SNSB), Canada (CSA), France (CNES), and Finland (Tekes). ACE/FTS is funded by the Canadian Space Agency. Support at Waterloo was also provided by the NSERC-Bomem-CSA-MSC Industrial Research Chair in Fourier Transform Spectroscopy. SORCE data are from the Laboratory for Atmospheric and Space Physics, Colorado.

References

1. J.G. Anderson. J. Geophys. Res. **76**, 7820 (1971).
2. M.F. Morgan, D.G. Torr, and M.R. Torr. Geophys. Res. Lett. **20**, 511 (1993).
3. R.R. Conway, M.H. Stevens, C.M. Brown, J.G. Cardon, S.E. Zasadil, and G.H. Mount. J. Geophys. Res. **104**, 16327 (1999).
4. R.R. Conway, M.E. Summers, M.H. Stevens, J.C. Cardon, P. Preusse, and D. Offermann. Geophys. Res. Lett. **27**, 2613 (2000).
5. M.H. Stevens and R.R. Conway. J. Geophys. Res. **104**, 16369 (1999).
6. M.E. Summers, R.R. Conway, R.E. Siskind, M.H. Stevens, D. Offermann, M. Riese, P. Preusse, D.F. Strobel, and J.M. Russell. Science, **277**, 1967 (1997).
7. K.W. Jucks, D.G. Johnson, K.V. Chance, W.A. Traub, J.J. Margitan, G.B. Osterman, R.J. Salawitch, and Y. Sasano. Geophys. Res. Lett. **25**, 2935 (1998).
8. R.P. Cageao, J.-F. Blavier, J.P. McGuire, Y. Jiang, V. Nemtchinov, F.P. Mills, and S.P. Sander. Appl. Opt. **40**, 2024 (2001).
9. K.-F. Li, R.P. Cageao, E.M. Karpilovsky, F.P. Mills, Y.L. Yung, J.S. Margolis, and S.P. Sander. Geophys. Res. Lett. **32**, L13813, doi:10.1029/2005GL022521 (2005).
10. E.J. Brinksma, Y.J. Meijer, I.S. McDermid, R.P. Cageao, J.B. Bergwerff, D.P.J. Swart, W. Ubachs, W.A. Matthews, W. Hogervorst, and J.W. Hovenier. Geophys. Res. Lett. **25**, 51 (1998).
11. U.-P. Hoppe, I. Baarstad, E.V. Thrane, T.A. Blix, R.P. Lowe, G.H. Hansen, and M. Gausa. LIDAR observations of a nocturnal hydroxyl layer in the upper mesosphere at high latitudes. EGS XXVI General Assembly. 25–29 March 2001. Nice, France. (http://www.copernicus.org/EGS/egsga/nice01/programme/abstracts/aai3169.pdf)
12. H.M. Pickett. Remote Sensing, **44**, 1122, doi:10.1109/TGRS.2005.862667, (2006).
13. H.M. Pickett, B.J. Drouin, T. Canty, L.J. Kovalenko, R.J. Salawitch, N. J.Livesey, W.G. Read, J.W. Waters, K.W. Jucks, and W.A. Traub. Geophys. Res. Lett. **33**, L01808, doi:10.1029/2005GL024048 (2006).
14. M.R. Schoeberl, A.R. Douglass, E. Hilsenrath, P.K. Bhartia, R. Beer, J.W. Waters, M.R. Gunson, L. Froidevaux, J.C. Gille, J.J. Barnett, P.F. Levelt, and P. DeCola. IEEE Trans. Geosci. Remote Sensing, **44**, 1066 (2006); doi:10.1109/TGRS.2005.861950.

15. R.L. Gattinger, D.A. Degenstein, and E.J. Llewellyn. J. Geophys. Res. **111**, D13303, doi:10.1029/2005JD006369 (2006).
16. E.J. Llewellyn, N.D. Lloyd, D.A. Degenstein, R.L. Gattinger, S.V. Petelina, A.E. Bourassa, J.T. Wiensz, E.V. Ivanov, I.C. McDade, B.H. Solheim, J.C. McConnell, C.S. Haley, C. von Savigny, C.E. Sioris, C.A. McLinden, E. Griffioen, J. Kaminski, W.F.J. Evans, E. Puckrin, K. Strong, V. Wehrle, R.H. Hum, D.J.W. Kendall, J. Matsushita, D.P. Murtagh, S. Brohede, J. Stegman, G. Witt, G. Barnes, W.F. Payne, L. Piché, K. Smith, G. Warshaw, D.-L. Deslauniers, P. Marchand, E.H. Richardson, R.A. King, I. Wevers, W. McCreath, E. Kyrölä, L. Oikarinen, G.W. Leppelmeier, H. Auvinen, G. Mégie, A. Hauchecorne, F. Lefèvre, J. de La Nöe, P. Ricaud, U. Frisk, F. Sjoberg, F. von Schéele, and L. Nordh. Can. J. Phys. **82**, 411 (2004).
17. D.P. Murtagh, U. Frisk, F. Merino, M. Ridal, A. Jonsson, J. Stegman, G. Witt, P. Eriksson, C. Jiménez, G. Megie, J. de la Noë, P. Ricaud, P. Baron, J.R. Pardo, A. Hauchcorne, E.J. Llewellyn, D.A. Degenstein, R.L. Gattinger, N.D. Lloyd, W.F.J. Evans, I.C. McDade, C.S. Haley, C. Sioris, C. von Savigny, B.H. Solheim, J.C. McConnell, K. Strong, E.H. Richardson, G.W. Leppelmeier, E. Kyrölä, H. Auvinen, and L. Oikarinen. Can J. Phys. **80**, 309 (2002).
18. P.F. Bernath, C.T. McElroy, M.C. Abrams, C.D. Boone, M. Butler, C. Camy-Peyret, M. Carleer, C. Clerbaux, P.-F. Coheur, R. Colin, P. DeCola, M. DeMazière, J.R. Drummond, D. Dufour, W.F.J. Evans, H. Fast, D. Fussen, K. Gilbert, D.E. Jennings, E.J. Llewellyn, R.P. Lowe, E. Mahieu, J.C. McConnell, M. McHugh, S.D. McLeod, R. Michaud, C. Midwinter, R. Nassar, F. Nichitiu, C. Nowlan, C.P. Rinsland, Y.J. Rochon, N. Rowlands, K. Semeniuk, P. Simon, R. Skelton, J.J. Sloan, M.-A. Soucy, K. Strong, P. Tremblay, D. Turnbull, K.A. Walker, I. Walkty, D.A. Wardle, V. Wehrle, R. Zander, and J. Zou. Geophys. Res. Lett. **32**, L15S01, doi:10.1029/2005GL022386 (2005).
19. T.J. Keneshea, P. Zimmerman, and C.R. Philbrick. Planet. Space Sci. **27**, 385 (1979).
20. M. Allen, J.I. Lunine, and Y.L. Yung. J. Geophys. Res. **89**, D3, 4841 (1984).
21. ECMWF (European Centre for Medium-Range Weather Forecasts). User Guide to ECMWF forecast products, Edition 3.1, Meteorological Bulletin M3.2. 6 August 2001.
22. S.P. Sander, R.R. Friedl, D.M. Golden, M.J. Kurylo, R.E. Huie, V.L. Orkin, G.K. Moortgat, A.R. Ravishankara, C.E. Kolb, M.J. Molina, and B.J. Finlayson-Pitts. Chemical kinetics and photochemical data for use in atmospheric studies, Jet Propulsion Laboratory Publications 02-25, Evaluation Number 14, 1 February 2003.
23. SORCE data. http://lasp.colorado.edu/sorce/data_access.html
24. G. Brasseur and S. Solomon. Aeronomy of the middle atmosphere. D. Reidel, Boston, Mass. 1984.
25. A.S. Medvedev and R.J. Greatbatch. J. Geophys. Res. **109**, D07104, doi:10.1029/2003JD003931 (2004).
26. B.V. Khattatov, V.A. Yudin, M.A Geller, and P.B. Hays. J. Geophys. Res. **102**, 4423 (1997).
27. W.E. Ward, J. Oberheide, M. Riese, P. Preusse, and D. Offermann. J. Geophys. Res. **104**, 16391 (1999).
28. C.D. Boone, R. Nassar, K.A. Walker, Y. Rochon, C.P. Rinsland, and P.F. Bernath. Appl. Opt. **44**, 7218 (2005).